Journal of Alloys and Compounds 649 (2015) 267–274

Contents lists available at ScienceDirect

Journal of Alloys and Compounds

journal homepage: http://www.elsevier.com/locate/jalcom

# Electrochemical and metallurgical characterization of $ZrCr_{1-x}NiMo_x$ $AB_2$ metal hydride alloys

Teliz Erika [a], Faccio Ricardo [b], Ruiz Fabricio [c, d], Zinola Fernando [a], Díaz Verónica [e, *]

[a] Universidad de la República, Facultad de Ciencias, Laboratorio de Electroquímica Fundamental, Núcleo Interdisciplinario Ingeniería Electroquímica, Igua 4225, CP 11400 Montevideo, Uruguay

[b] Universidad de la República, Crystallography, Solid State and Materials Laboratory (Cryssmat-Lab), DETEMA, Centro NanoMat, Polo Tecnológico de Pando, Espacio Interdisciplinario, Facultad de Química, Montevideo, Uruguay

[c] Consejo Nacional de Investigaciones Científicas y Técnicas, CONICET, Av. Rivadavia 1917, C1033AAJ Ciudad de Buenos Aires, Argentina

[d] Centro Atómico Bariloche, Comisión Nacional de Energía Atómica (CAB-CNEA), Av. Bustillo 9500, CP 8400 S.C. de Bariloche, RN, Argentina

[e] Universidad de la República, Facultad de Ingeniería, Instituto de Ingeniería Química, Núcleo Interdisciplinario Ingeniería Electroquímica, J.Herrera y Reissig 565, CP 11300 Montevideo, Uruguay

ARTICLE INFO

*Article history:*
Received 12 June 2015
Received in revised form
20 July 2015
Accepted 21 July 2015
Available online 23 July 2015

*Keywords:*
Molybdenum
Metal hydrides
Laves phase
$Zr_xNi_y$
Hydrogen

ABSTRACT

The effects of partial replacement of chromium by molybdenum was studied on the structure and electrochemical kinetic properties of $ZrCr_{1-x}NiMo_x$($x$ = 0.0, 0.3 and 0.6) metal hydride alloys. The arc-melting prepared alloys were metallurgically characterized by X-ray diffraction and energy dispersive spectroscopy microanalysis, which showed $AB_2$ (with hexagonal C14 structure) and $Zr_xNi_y$ ($Zr_7Ni_{10}$, $Zr_9Ni_{11}$) phases. After a partial substitution of chromium by molybdenum, secondary phases monotonically increase with the C14 unit cell volume indicating that most of molybdenum atoms locate in the B-site.

The alloys were electrochemically characterized using charge/discharge cycling, electrochemical impedance spectroscopy and rate capability experiments that allowed the determination of hydriding reaction kinetic parameters. The presence of molybdenum produces a positive effect for hydrogen diffusion in the alloy lattice, and $ZrCr_{0.7}NiMo_{0.3}$ alloy depicts the better kinetics associated with a fast activation, lower charge transfer resistance and the best high rate discharge behavior. This fact would be related to a lower diffusion time constant and a bigger value of the product between exchange density current and surface active area. There is a trade-off in the amounts of secondary phase and Laves phases in order to improve the kinetic performance.



## 1. Introduction

One of the most used technologies in hybrid electrical vehicles (HEVs) are nickel metal hydride (Ni/MH) batteries. Although having a disadvantage in its low specific energy, they are safe and stable with a useful price. $AB_2$ metal hydride alloys were proposed as the candidates to substitute the present commercial $AB_5$-type alloys to increase the discharge capacity [1–3]. $AB_2$ alloys employed as the negative electrode in Ni/MH batteries are multi-element (like Zr and Ti for A atom and Cr, Ni, Mn and V for B atom), and multi-phase materials (integrated for Laves phases and secondary non-Laves phases) [1–6]. It was demonstrated that the electrocatalytic performance of Zr-based alloys are based on the presence of $Zr_8Ni_{21}$, $Zr_7Ni_{10}$, $Zr_9Ni_{11}$ and ZrNi as secondary phases [7–11]. These electrodes need several charge–discharge cycles to achieve the maximum capacity and also show bad high rate discharge (HRD) behaviors. In order to enhance the kinetic and thermodynamic properties of electrodes, a number of methods have been applied before, such as, partial substitution, different element incorporation in the alloy composition, surface chemical treatment and different phases and rare earths or nickel powder additions [12–16]. Diverse investigations have found that elements such as copper, iron and molybdenum enhanced the $AB_2$ MH performance [17–21]. The addition of a small amount of molybdenum in the $AB_2$ alloy system induces a positive effect, increasing hydrogen storage capacity, improving activation characteristics, leading a maximum discharge capacity, and increasing cyclic durability [22,23]. Moreover, molybdenum containing

* Corresponding author.
*E-mail address:* verodiaz@fing.edu.uy (D. Verónica).

http://dx.doi.org/10.1016/j.jallcom.2015.07.206
0925-8388/

alloys, lowers the plateau pressure, changes the microstructures of the alloys and increases the surface porosity [24–27]. Probably, these facts induce a large effect on the electrochemical properties of alloy electrodes [25]. However, other studies reveled that molybdenum addition shortens the cycle life [28–30], decreases high-rate dischargeability behavior, increases self-discharge rate and the charge-transfer resistance at the surface of the alloy electrodes [23]. Since the results of $AB_2$ molybdenum containing alloys behavior seem to be inconsistent, our investigation was focused on structural and electrochemical kinetic studies of molybdenum content in a simple $AB_2$ metal hydride alloys.

## 2. Experimental

### 2.1. Synthesis of alloys

The alloys were prepared by arc melting with adequate proportions of the composition elements (purity better than 99.9%) inside a copper-cooled hearth under high purity argon (99.998%). The alloys were remelted for the purpose of homogenization. After then, they were mechanically pulverized them for the electrode formation.

For the electrochemical characterization, the electrodes were prepared by compacting a mixture of 100 mg of sample powders with equal amounts of teflonized carbon (Vulcan XC-72), inside a cylindrical device to a pressure of 250 MPa at room temperature, resulting a total electrode surface of 2 $cm^2$(geometrical area) and a thickness around 1 mm. A nickel wire was used as current collector. Further details of electrode preparation can be revised in Petrov's work [31]. Four alloys were synthesized replacing chromium by molybdenum ($ZrCr_{1-x}NiMo_x$): $AB_2M0$ (Mo 0% w/w), $AB_2M1$ (Mo 13% w/w) and $AB_2M2$ (Mo 25% w/w).

### 2.2. Structural and microstructural characterization of MH electrodes

The prepared electrodes were characterized by X-ray diffraction using a Rigaku ULTIMA IV, 285 mm radius, powder diffractometer operating in Bragg Brentano geometry. $CuK_\alpha$ radiation ($\lambda = 1.5418$ Å), monochromatized with a diffracted beam bent germanium crystal, was used to collect data over the 10–110° 2θ range, in steps of 0.02°, using a scintillation detector. Fixed slits of 2/3° were used for data collection to prevent beam spillage outside the 2 cm long sample (along the beam-path) at low angles. The first step consisted of identifying the composition of the samples and the determination of the structures, which were similar in cell parameters and symmetry. After this, the structural models for the full pattern profile fitting were prepared, using the Rietveld method [32] by means of the EXPGUI-GSAS suite [33,34]. This methodology allowed extracting precise and relevant structural parameters and corresponding weight crystalline fraction in the case of multiphase systems.

**Table 1**
Atomic ratio corresponding to the different phases in $AB_2$ M0, $AB_2$ M1, $AB_2$ M2 alloys from energy dispersive spectroscopy studies (See Fig. 1).

| | Zr | Cr | Ni | Mo |
|---|---|---|---|---|
| $AB_2$ M0 (I) | 1 | 0.04 | 0.94 | 0 |
| $AB_2$ M0 (II) | 1 | 0.63 | 0.82 | 0 |
| $AB_2$ M0 (III) | 1 | 7.55 | 0.59 | 0 |
| $AB_2$ M1(I) | 1 | 0.06 | 0.88 | 0.05 |
| $AB_2$ M1 (II) | 1 | 0.59 | 0.62 | 0.27 |
| $AB_2$ M2 (I) | 1 | 1.92 | 0.23 | 6.05 |
| $AB_2$ M2 (II) | 1 | 0.04 | 0.91 | 0.07 |

Before electrochemical testing of electrodes, the surface alloy microstructures were examined by means of a scanning electron microscope (SEM, JEOL JSM 5900) employing a 25 kV secondary electron imaging mode and energy dispersive spectroscopy (EDS) microanalysis.

### 2.3. Electrochemical characterization

The hydride forming electrodes were mounted as detailed elsewhere [31], pressing the mixture onto a nickel mesh at room temperature.

Electrochemical measurements were run in a three-compartment cell placing the working electrode (metal hydride electrode), counter electrode (nickel mesh) and reference electrode (Hg/HgO electrodes). In this work, potentials are referred to the Hg/HgO reference electrode and all the experiments carried out at room temperature. The electrolyte, 6 M KOH solution, was prepared from reagent grade KOH and Millipore-MilliQ® plus water. Before performing the electrochemical impedance spectrum (EIS) measurements, the electrodes were charge–discharge cycled at constant current for 40 cycles.

During charge–discharge experiments, constant density currents of −80 mA/g and 26 mA/g were used respectively, with a charge time of 5 h and a cut-off potential of −0.6 V, during discharge. After cycling the electrodes, they were discharged to a state of charge (SOC) of 70%, and left at open circuit potential ($E_{ocp}$). The EIS spectra were recorded, at $E_{ocp}$, in the 50 kHz–1 mHz frequency range, with a 6 mV amplitude, ten points per decade. Zview program was employed in order to fit EIS experimental data.

High rate capability (HRD) experiments were performed at discharge rates in the 0.1C to 1C range. The currents were often related to the maximum discharge capacity of the electrode using the $C_{rate}$. The $C_{rate}$ can be calculated using the following equation;

$$C_{rate}\left[\frac{1}{h}\right] = \frac{I[mA/g]}{C_{\max,dc}[mAh/g]} \tag{1}$$

where$C_{max,dc}$ is the maximum discharge capacity.

All the electrochemical experiments were performed using a PGZ 301 Voltalab® potentiostat-galvanostat device.

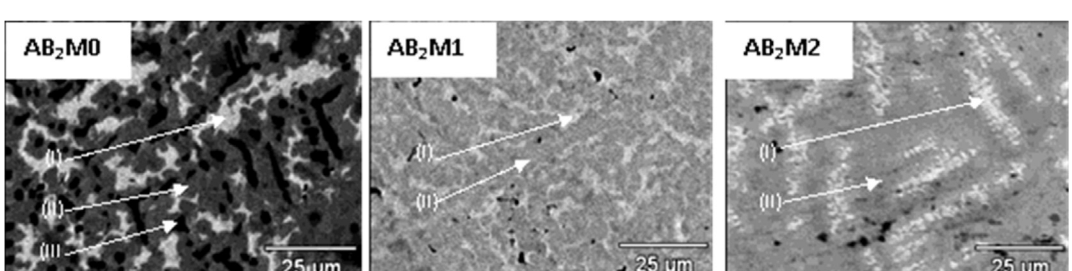


**Fig. 1.** SEM back-scatted electron micrographs for studied alloys. I, II and III indicate the different phases reported in Table 1.

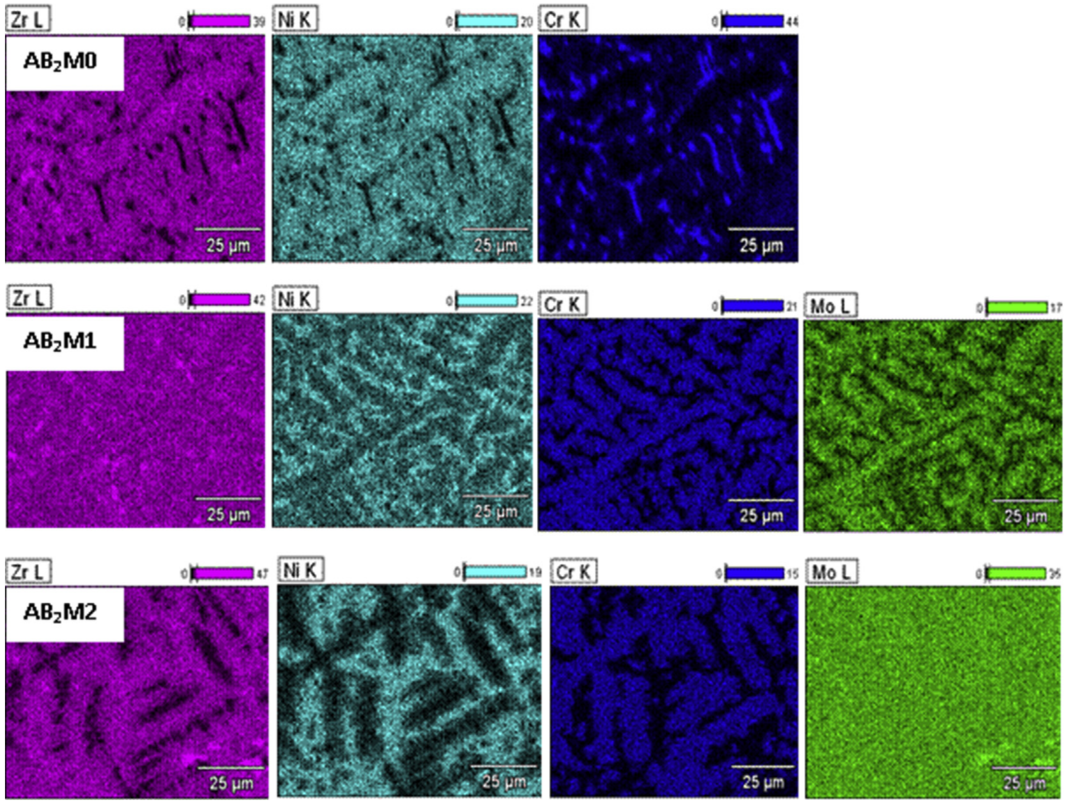


**Fig. 2.** EDS mapping studies for $AB_2M0$, $AB_2M1$ and $AB_2M2$ alloys.

## 3. Results and discussion

### 3.1. Metallurgical characterization

The microstructures of $ZrCr_{1\text{-}x}NiMo_x$ with $AB_2M0$ (Mo 0% w/w), $AB_2M1$ (Mo 13% w/w) and $AB_2M2$ (Mo 25% w/w) alloys were studied by SEM (back-scattered electrons, BSE) (Fig. 1). Samples were mounted and polished on epoxy blocks; Table 1 depicts the results of several EDS analysis performed on different sample regions, concluding that the stoichiometry for the three alloys studied was the expected one. The microstructure investigation presented in Fig. 1 shows a main matrix and one or two segregated phases (light gray (I), gray(II) and dark gray(III)). The alloys are mainly composed of $AB_2$ (with B/A around 2.0) and $Zr_xNi_y$ phases. There is one high-chromium phase found in $AB_2M0$ alloy (phase III in Fig. 1). All phases are randomly distributed within the matrix. The analyzed mapping elements are presented in Fig. 2.

XRD patterns shown in Fig. 3, reflect the existence of the phases reported in Table 2. Almost all peaks can be fitted into a hexagonal C14 structure ($MgZn_2$ type, Space group $P6_3/mmc$) and $Zr_xNi_y$ phases (can be $Zr_7Ni_{10}$, $Zr_9Ni_{11}$). The lattice constants, *a* and *c*, determined from the XRD patterns are listed in Table 2. As the amount of Mo increases, both *a* and *c for Laves phases* increase due to the larger Mo atomic radius [34–37]. This is proof that most molybdenum atoms locate in the B-site, because this element is smaller than zirconium, but larger than chromium (B-site element). If most of molybdenum atoms substitute zirconium in the A-site, the lattice constants will significantly be reduced. The unit cell volume of hexagonal structure (Space group $P6_3/mmc$) also increases as molybdenum content raises. $AB_2$ M2 alloy presents insignificant amounts of $Mo_{1\text{-}x}M_x$ alloy cubic phase with Im-3m space group, being M other metals. These outcomes are in accordance to EDS results where molybdenum is seeing to be homogeneously distributed (see Fig. 2). Due to the very low crystalline contribution, this phase is not included in data reported in Table 2.

For $AB_2$ Zr/Ni based alloys, secondary non-Laves phases developed in addition to the main Laves phases, being $Zr_7Ni_{10}$, $Zr_9Ni_{11}$, the one observed here. It is worth noticing that kinetics and thermodynamic behavior negatively affected after removing the secondary phases. The electrocatalytic properties deteriorate due to the reduction of synergetic effects between the main storage and secondary non Laves phases [7,14,38–42]. The term "synergetic effect" employed by Nei et al. [43], is used to describe the discharge capacity enhancements or high-rate dischargeability (HRD)

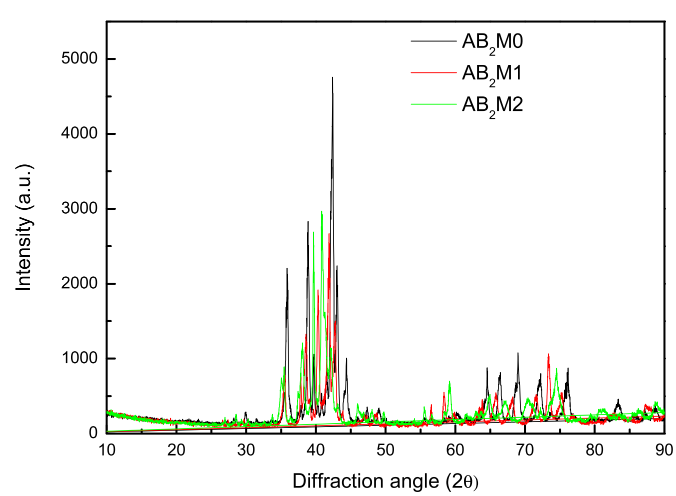


**Fig. 3.** X-ray diffraction patterns for $AB_2M0$, $AB_2M1$ and $AB_2M2$ alloys.

**Table 2**
-Results obtained from the Full Profile Pattern Refinement obtained from the Rietveld Method. Cell parameters, Space Group, Fraction Weight and statistical resume for samples $AB_2$ M0, $AB_2$ M1 and $AB_2$ M2.

| | | $AB_2M0$ | $AB_2M1$ | $AB_2M2$ |
|---|---|---|---|---|
| Laves Phase | Space Group | $AB_2$:P6$_3$/m m c | $AB_2$:P6$_3$/m m c | $AB_2$:P6$_3$/m m c |
| | a(Å) | 5.0167 | 5.0579 | 5.1067 |
| | b(Å) | 5.0167 | 5.0579 | 5.1067 |
| | c(Å) | 8.2170 | 8.2708 | 8.3795 |
| | V(Å$^3$) | 179.10 | 183.24 | 189.249 |
| | Weight (%) | 94.5(5) | 69.5(3) | 35.5(3) |
| $Zr_xNi_y$ Phase | Space Group | $Ni_{11}Zr_9$: I4/m | $Ni_{10}Zr_7$: Pbca | $Ni_{11}Zr_9$: I4/m |
| | a(Å) | 9.8945 | 12.3523 | 9.8443 |
| | b(Å) | 9.8945 | 9.1985 | 9.8443 |
| | c(Å) | 6.6053 | 9.1916 | 6.6134 |
| | V(Å$^3$) | 646.67 | 1044.37 | 640.913 |
| | Weight (%) | 5.5(5) | 30.5(3) | 64.5(3) |
| Statistical Parameters | wRp | 0.2199 | 0.2801 | 0.2142 |
| | Rp | 0.1619 | 0.2052 | 1.1629 |
| | R(F$^2$) | 0.3341 | 0.5869 | 0.3640 |
| | Nobs | 464 | 1051 | 462 |
| | $\chi^2$ | 13.51 | 17.80 | 12.04 |

positively contributing to the overall performance of the $AB_2$ phase in the presence of $Zr_xNi_y$. The occurrence of these phases offers additional catalytic sites for the gaseous phase hydrogen storage and electrochemical reactions [38–42]. Consequently, understanding these secondary phases behavior is crucial for future development of $AB_2MH$ alloys. It can be observed that partial replacement of chromium by molybdenum (in the studied amounts) promotes the segregation of $Zr_xNi_y$ phase.

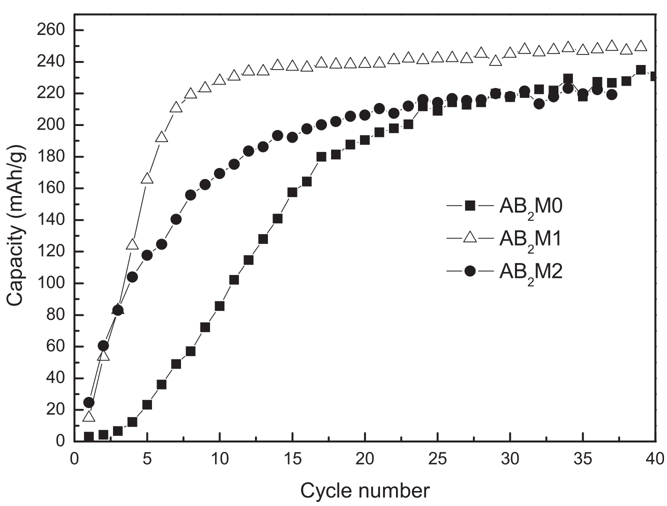


**Fig. 4.** Discharge capacities as a function of charge–discharge cycle number for $AB_2M0$, $AB_2M1$, and $AB_2M2$ alloys at current density of 26 mA/g.

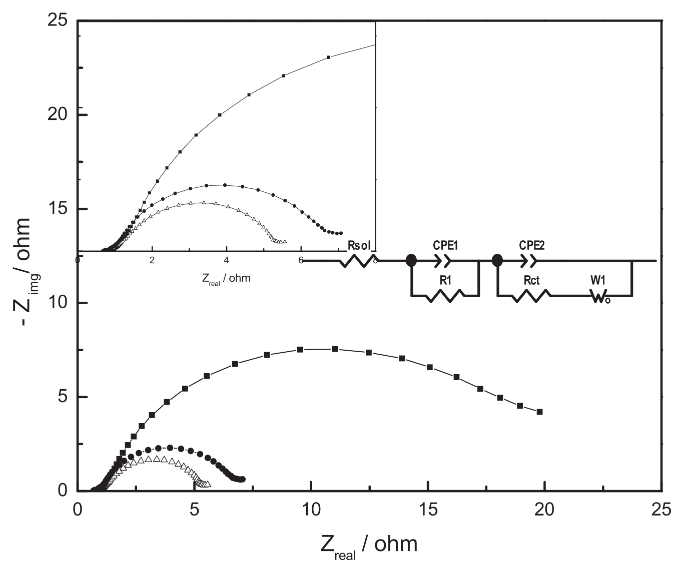


**Fig. 6.** Nyquist plot for 70% state of charge (SOC): $AB_2M0$ (full squares), $AB_2M1$ (open triangles), and $AB_2M2$ (full circles) alloys.

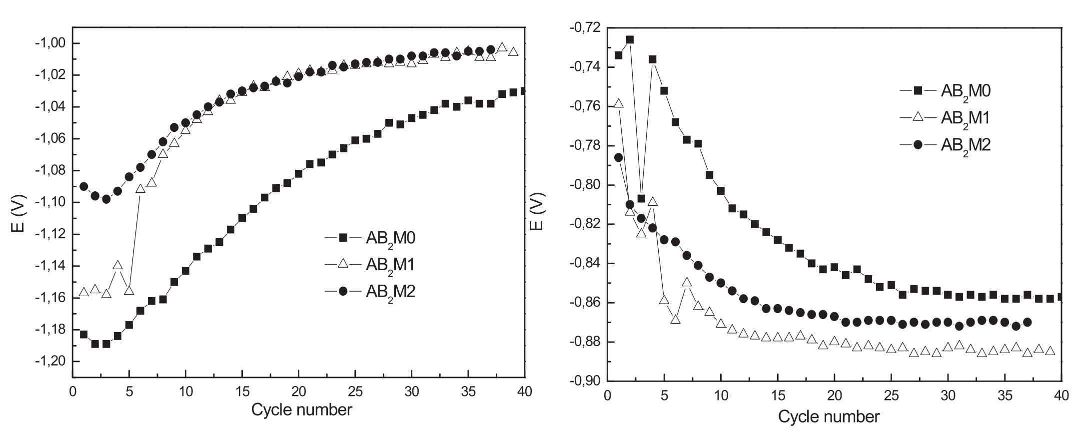


**Fig. 5.** Charge ending potential (left) and half discharge potential (right) as a function of charge–discharge cycle number for $AB_2M0$, $AB_2M1$, and $AB_2M2$ alloys.

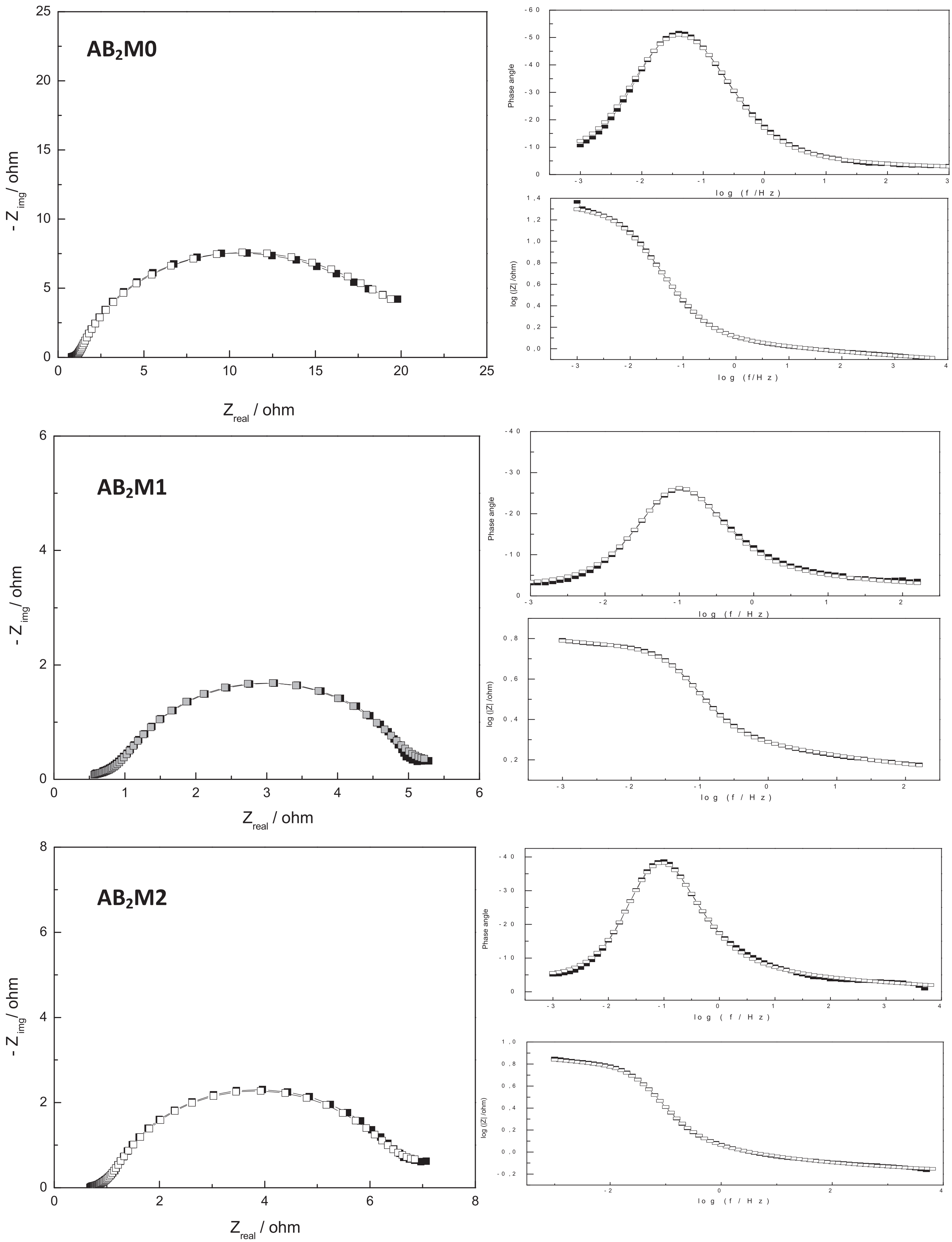


**Fig. 7.** Experimental (open squares) and modeled (full squares) data in Nyquist and Bode (Module and Phase) plots for $AB_2M0$, $AB_2M1$ and $AB_2M2$ alloys.

### 3.2. Electrochemical characterization

The discharge capacities of the alloys samples are plotted as a function of the number of charge–discharge cycles in Fig. 4. It is worthwhile that maximum capacity values for $AB_2M0$, $AB_2M1$ and $AB_2M2$ are similar.

$AB_2M1$ alloys required less number of cycles for reaching a stabilized full discharge capacity, leading to a faster activation. Many studies indicate that the number of activation cycles increases with the increase of the Zr/Ni ratio [9,40–43]. $AB_2M1$ alloy has $Zr_7Ni_{10}$ as secondary phases in contrast to $AB_2M0$ and$AB_2M2$ alloys which have $Zr_9Ni_{11}$, which is in accordance with these results.

The evolution of charge ending potential and half-discharge potential with the number of charge–discharge cycles is presented in Fig. 5. It can be observed that $AB_2M1$ has a charging potential closer to the reversible value than that of the $AB_2M0$ sample. Considering the half-discharge potential, it has also been found than $AB_2M1$ rapidly approaches to the reversible potential. Hence, overpotential values decrease with growing the cycle number for all samples, except for the very initial sets. The decrease in the overpotential is more significant in $AB_2M1$ alloy and this sample also depicts the lowest overpotential value.

Fig. 6 shows Nyquist plot and the electric equivalent circuit of $AB_2$ alloy electrodes with two depressed semicircles. The studied alloys display a distorted semicircle at high frequencies which is associated with different facts such the contact resistances between the current collector and the alloy, particle-to particle resistance, contact surfaces and oxide layer thickness [44–46], etc. It is worth noticing that, up to now, researches do not agree with the source assignment of this small semicircle.

The second capacitive response is associated to the interface capacity relaxation in parallel with the charge transfer resistance ($\boldsymbol{R_{ct}}$). As it can be observed, $AB_2M1$ depicts the smallest semicircle diameter, indicating that this sample has the lowest $\boldsymbol{R_{ct}}$ value. As a result, it can be concluded that $AB_2M1$ has the largest value for the product between exchange density current and surface active area ***($j_0$ * $A_a$)***. Therefore, $AB_2M1$ depicts the best electrocatalytic properties for the hydriding processes. Fig. 6 also shows the equivalent electric circuit for EIS data of metal hydride electrodes. It consists of at least four components: electrolyte resistance, two resistive components and a Warburg term.

Nyquist and Bode diagrams for experimental and fitting data are depicted in Fig. 7. From Warburg parameters' values diffusion specific time constants were calculated, the term $\boldsymbol{W_T}$ is defined as $\boldsymbol{R^2/D}$, being $\boldsymbol{R}$ the particle radius and $\boldsymbol{D}$ the diffusion coefficient. The smallest diffusion time constant is for $AB_2M1$, whereas the biggest Warburg resistant ($\boldsymbol{W_R}$) is obtained for $AB_2M0$ (see Table 3). These results indicate that hydrogen diffusion occurs easier in $AB_2M1$ than in $AB_2M0$ samples. Moreover, the formation of secondary phases affects hydrogen diffusion paths from surface to metal bulk.

Fig. 8 presents high-rate discharge curves. For 1C rate discharge $AB_2M1$ depicts 80% of its maximum capacity and $AB_2M2$ 55% of its maximum discharge capacity. However, molybdenum-non containing alloy ($AB_2M0$) retained only 35% of it. The improvement in HRD can possibly be attributed to the presence of secondary phases, which enables the bulk hydrogen diffusion in the alloy. The $AB_2/Zr_xNi_y$ can be related with the higher or smaller bulk diffusion constant. For analyzing hydrogen transfer rate in the alloy, and comparison of hydrogen diffusion specific time constant value with that resulted from EIS model, we are going to use analytical solutions derived from second Fick's law assuming a spherical shape for the particle alloy:

$$\frac{d(RC_H)}{dt} = D_H \frac{\partial^2 (RC_H)}{\partial R^2} \quad (2)$$

where$C_H$ is the hydrogen concentration in the alloy, $\boldsymbol{t}$ is time,$D_H$ is an average hydrogen diffusion coefficient, $\boldsymbol{R}$ is the distance from the center of the sphere to the bulk of the material. Supposing a uniform initial hydrogen concentration in the bulk of the alloy and constant surface concentration for large times, Eq. (2) reduces to the hydrogen current intensity,$I_H(t)$, time dependent expression [47]:

$$I_H(t) = F\frac{D_H \Delta C_H}{\delta R^2} - \frac{\pi^2 D_H}{R^2} C(t) \quad (3)$$

With $\delta$ the width of the diffusion layer, F the Faraday's constant and $C(t)$ the capacity of the alloy

$$C(t) = \int_0^t I_H(t)dt \quad (4)$$

From Eq. (3), $\boldsymbol{R^2/D}$ may be evaluated from the slope of the curves plotted in Fig. 8, where it is clear for $AB_2M0$ alloy depicts two distinct slopes. Thus, in order to calculate diffusion time constant for long time experiments, additional tests were run in $\boldsymbol{C_{rate}}$ ranging from 0.05 to 0.3C. Table 4 shows these results which are clearly similar to those resulting from EIS modeling, being the $AB_2M1$ diffusion time constant the lowest one of all.

In general, the main reaction steps during charging/discharging processes or hydrogen absorption/evolution reactions are:

$$H_2O + M + e^- \leftrightarrow [MH]_{ads} + OH^- \quad \text{(I)} \quad \text{volmer reaction}$$

$$[MH]_{ads} + H_2O + e^- \leftrightarrow M + H_2 + OH^- \quad \text{(II)} \quad \text{Heyrovsky reaction}$$

$$2[MH]_{ads} \leftrightarrow 2M + H_2 \quad \text{(III)} \quad \text{Tafel reaction}$$

$$[MH]_{ads} \leftrightarrow \{MH\}_{abs} \quad \text{(IV)} \quad \text{Hydrogen absorption step}$$

$$\{MH\}_{abs} \rightarrow MH_{bulk} \quad \text{(V)} \quad \text{Diffusion step}$$

$$MH_{(\alpha)} \leftrightarrow MH_{(\beta)} \quad \text{(VI)} \quad \text{Transformation from}(\alpha) \text{ to } (\beta) \text{ phase}$$

Volmer step denotes the charge transfer reaction at the surface of the alloy particles. Thus, the electrochemical reaction of hydrogen absorption/evolution process is strongly dependent on the surface of the alloy particle. On the other hand, the structure characteristic of the metal hydrides determines the hydrogen diffusion rate in the bulk of the alloys [48]. Reaction (IV) represents the reversible transport of hydrogen from adsorption sites on the electrode surface to absorption sites in the near-surface region [49]. (V) step characterizes the diffusion of absorbed hydrogen from the nearby-surface region to metal bulk. This route denotes the gradual transfer of hydrogen atoms diffusing into the alloy bulk and

**Table 3**
EIS parameters $R_{ct}$, $W_R$, $W_T$ and ($j_o \times a$) for $AB_2M0$, $AB_2M1$ and $AB_2M2$ alloys obtained from the equivalent electric circuit shown in the inset of Fig. 6.

| | $R_{ct}(\Omega)$ | $W_R\ (\Omega)$ | $W_T(s)$ | $j_o \times a\ (Acm^{-3})$ |
|---|---|---|---|---|
| $AB_2M0$ | 17,5 | 23 | 2,5E+04 | 1,5E-03 |
| $AB_2M1$ | 3,4 | 1 | 8,0E+03 | 7,5E-03 |
| $AB_2M2$ | 4,6 | 1 | 1,0E+04 | 5,5E-03 |

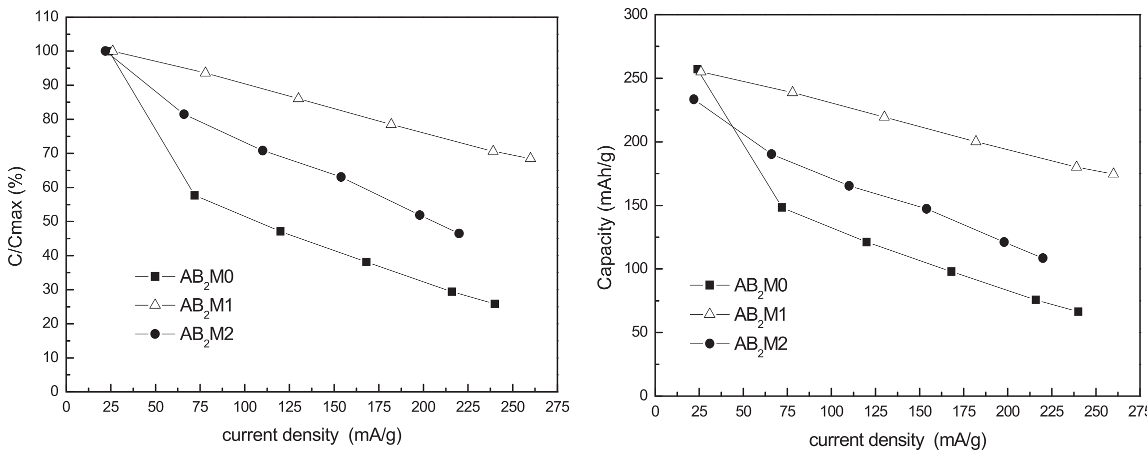


**Fig. 8.** High rate discharge (HRD) curves expressed as a percentage of maximum capacity and in mAh/g for $AB_2M0$, $AB_2M1$, and $AB_2M2$ alloys.

occupying the interstitial sites in the crystal structure. After then, the transformation from metal–solution (α) phase to hydride (β) phase occurs.

Thus, it can be concluded from experimental results that hydrogen diffusion is likely to be the rate-limiting step of the charging/discharging reaction in the $AB_2$ alloy.

## 4. Conclusions

a. - The stoichiometry for $AB_2$ alloys experimentally found is similar to the theoretical composition.
b. - Metallurgical characterization evidences the presence of segregated $Zr_xNi_y$ type, as well as hexagonal C14 structures. The partial replacement of chromium by molybdenum promotes the segregation of $Zr_xNi_y$ phase.
c. - $AB_2M1$-molybdenum containing alloy depicts the best kinetics performance as a result of a fast activation, lower $\boldsymbol{R_{ct}}$ (EIS studies) and the best HRD behavior. This enhancement is attributed to the higher diffusion coefficient and bigger $(\boldsymbol{j_0 * A_a})$ parameter, improving the hydriding processes.
d. - The specific diffusion time constant for $AB_2M1$ alloys is the smallest one. Besides, values calculated from HRD experiments are similar to those analyzed from equivalent electric circuit in EIS.
e. - The incorporation of molybdenum to the alloys has a helpful impact in hydrogen diffusion process within the alloy lattice.
f. - Electrochemical experiments demonstrate the catalytic effect of segregated phases on the electrochemical hydrogen absorption properties of $AB_2$ alloys.
g. - The large hydrogen diffusivity observed in $AB_2M1$ is the consequence of the generation of an adequate path as a consequence of secondary phase's segregation in straight connection with $AB_2$ phase. Therefore, there is a trade-off in the amounts of secondary phase and Laves phases in order to improve thermodynamic and kinetic performances.

**Table 4**
Retaining percentage in $C_{rate}$ range 0.05–0.3C and diffusion time constant, as $R^2/D$, for $AB_2M0$, $AB_2M1$ and $AB_2M2$ alloys.

| | $AB_2M0$ | $AB_2M1$ | $AB_2M2$ |
|---|---|---|---|
| $C_{rate}0.05$ | 100 | 100 | 100 |
| $C_{rate}0.10$ | 93 | 99 | 95 |
| $C_{rate}0.15$ | 88 | 99 | 90 |
| $C_{rate}0.20$ | 84 | 99 | 87 |
| $C_{rate}0.25$ | 78 | 98 | 81 |
| $C_{rate}0.30$ | 73 | 97 | 77 |
| $R^2/D$ | 3,8E+04 | 4,2E+03 | 3,5E+04 |

## Acknowledgments

The authors acknowledge Bach. C. Yattah her collaboration in some electrochemical experiments. The authors acknowledge ANII and CSIC projects for the financial support. C.F. Zinola, V. Díaz and R. Faccio are researchers at PEDECIBA/United Nations. C.F. Zinola is a member of the Electrochemical Society.

## References

[1] S.R. Ovshinsky, M.A. Fetcenko, J. Ross, A nickel metal hydride battery for electric vehicles, Science 260 (1993) 176–181.
[2] M.A. Fetcenko, S.R. Ovshinsky, K. Young, B. Reichman, C. Fierro, J. Koch, F. Martin, W. Mays, T. Ouchi, B. Sommers, A. Zallen, High catalytic activity disordered VTiZrNiCrCoMnAlSn hydrogen storage alloys for nickel–metal hydride batteries, J. Alloys Compd. 330/332 (2002) 752–759.
[3] M.A. Fetcenko, S.R. Ovshinsky, B. Reichman, K. Young, C. Fierro, J. Koch, A. Zallen, W. Mays, T. Ouchi, Recent advances in NiMH battery technology, J. Power Sources 165 (2007) 544–551.
[4] K. Young, B. Chao, Y. Liu, J. Nei, Microstructures of the oxides on the activated AB2 and AB5 metal hydride alloys surface, J. Alloys Compd. 606 (2014) 97–104.
[5] K. Young, T. Ouchi, B. Huang, B. Reichman, M.A. Fetcenko, The structure, hydrogen storage, and electrochemical properties of Fe-doped C14-predominating $AB_2$ metal hydride alloys, Int. J. Hydrogen Energy 36 (2011) 12296–12304.
[6] K. Young, T. Ouchi, A. Banik, J. Koch, M.A. Fetcenko, Improvement in the electrochemical properties of gas atomized $AB_2$ metal hydride alloys by hydrogen annealing, Int. J. Hydrogen Energy 36 (2011) 3547–3555.
[7] K. Young, J. Nei, T. Ouchi, M.A. Fetcenko, Phase abundances in $AB_2$ metal hydride alloys and their correlations to various properties, J. Alloys Compd. 509 (2011) 2277–2284.
[8] K. Young, T. Ouchi, B. Huang, B. Reichman, M.A. Fetcenko, Effect of molybdenum content on structural, gaseous storage, and electrochemical properties of C14-predominant $AB_2$ metal hydride alloys, J. Power Sources 20 (2011) 8815–8821.
[9] F.C. Ruiz, E.B. Castro, H.A. Peretti, A. Visintin, A Study of the different $Zr_xNi_y$ phases of Zr-based $AB_2$ materials, Int. J. Hydrogen Energy 35 (2010) 9879–9887.
[10] D. Escobar, S. Srinivasan, Y. Goswami, E. Stefanakos, Hydrogen storage behavior of ZrNi 70/30 and ZrNi 30/70 composites, J. Alloys Compd. 458 (2008) 223–230.
[11] K. Young, M. Young, S. Chang, B. Huang, Synergetic effects in electrochemical properties of $ZrV_xNi_{4.5-x}$ (x = 0.0, 0.1, 0.2, 0.3, 0.4, and 0.5) metal hydride alloys, J. Alloys Compd. 560 (2013) 33–41.
[12] C.B. Jung, J.H. Kim, K.S. Lee, Electrode characteristics of nanostructured TiFe and $ZrCr_2$ type metal hydride prepared by mechanical alloying, Nanostructured Mater 8 (1997) 1093–1104.
[13] A.R. Santos, R.C. Ambrosio, E.A. Ticianelli, Electrochemical and structural studies on nonstoichiometric $AB_2$-type metal hydride alloys, Int. J. Hydrogen Energy 29 (2004) 1253–1261.
[14] A. Visintin, H.A. Peretti, F.C. Ruiz, H.L. Corso, W.E. Triaca, Effect of additional

catalytic phases imposed by sintering on the hydrogen absorption behavior of $AB_2$ type Zr-based alloys, J. Alloys Compd. 428 (2007) 244–251.
[15] S.M. Han, Z. Zhang, M.S. Zhao, M. Zheng, Electrochemical characteristics and microstructure of $Zr_{0.9}Ti_{0.1}Ni_{1.1}Mn_{0.6}V_{0.3}$-$LaNi_5$ composite hydrogen storage alloys, Int. J. Hydrogen Energy 31 (2006) 563–567.
[16] Y.H. Zhang, P. Li, X.Y. Wang, Y.F. Lin, G. Wang, The effects of rapid quenching on the electrochemical characteristics and microstructures of $AB_2$ Laves phase electrode alloys, J. Power Sources 128 (2004) 90–96.
[17] S. Kim, H. Lee, K. Cho, J. Lee, Effect of Cu powder as an additive material on the inner pressure of a sealed-type Ni–MH rechargeable battery using a Zr-based alloy as an anode, J. Alloys Compd. 282 (1999) 261–267.
[18] K. Young, T. Ouchi, A. Banik, J. Koch, M.A. Fetcenko, L.A. Bendersky, K. Wang, Gas atomization of Cu-modified AB5 metal hydride alloys, J. Alloys Compd. 509 (2011) 4896–4904.
[19] H. Yang, Y. Chen, M. Tao, C. Wu, J. Shao, G. Deng, Low temperature electrochemical properties of $LaNi_{4.6-x}Mn_{0.4}M_x$ (M = Fe or Co) and effect of oxide layer on EIS responses in metal hydride electrodes, Electrochim. Acta 55 (2010) 648–655.
[20] P.H.L. Notten, P. Hokkeling, Double-Phase hydride forming compounds: A new class of highly electrocatalytic materials, J. Electrochem. Soc. 138 (1991) 1877–1885.
[21] H. Senoh, Y. Hara, H. Inoue, C. Iwakura, Charge efficiency of misch metal-based hydrogen storage alloy electrodes at relatively low temperatures, Electrochim. Acta 46 (2001) 967–971.
[22] M. Au, F. Pourarian, S.G. Sankar, W.E. Wallace, L. Zhang, $TiMn_2$-based alloys as high hydrogen storage materials, Mater Sci. Eng. B 33 (1995) 53–57.
[23] S. Li, M. Zhao, L. Wang, Y. Liu, Y. Wang, Structures and electrochemical characteristics of $Ti_{0.26}Zr_{0.07}V_{0.24}Mn_{0.1}Ni_{0.33}Mo_x$ (x = 0-0.1) hydrogen storage alloys, Mater Sci. Eng. B 150 (2008) 168–174.
[24] T. Huang, Z. Wu, B. Xia, N. Xu, Influence of stoichiometry and alloying elements on the crystallography and hydrogen sorption properties of TiCr based alloys, Mater Sci. Eng. A 397 (2005) 284–287.
[25] J. Chen, S.X. Dou, H.K. Liu, Hydrogen desorption and electrode properties of $Zr_{0.8}Ti_{0.2}(V_{0.3}Ni_{0.6}M_{0.1})_2$, J. Alloys Compd. 256 (1997) 40–44.
[26] T.P. Yadav, R. Shahi, O.N. Srivastava, Synthesis, characterization and hydrogen storage behaviour of $AB_2(ZrFe_2$, $Zr(Fe_{0.75}V_{0.25})_2$, $Zr(Fe_{0.5}V_{0.5})_2$ type materials, Int. J. Hydrogen Energy 37 (2012) 3689–3696.
[27] C. Jeong, W. Chung, C. Iwakura, I. Kim, Effect of temperature on the discharge capacity of the Laves phase alloy used in nickel/metal-hydride batteries, J. Power Sources 79 (1999) 19–24.
[28] M.Y. Song, I.H. Kown, D.S. Ahn, M.S. Sohn, Improvement in the electrochemical properties of $ZrMn_2$ hydrides by substitution of elements, Met. Mater. Int. 7 (2001) 257–263.
[29] M.Y. Song, D. Ahn, I.H. Kwon, S.H. Chough, Development of $AB_2$-Type Zr-Ti-Mn-V-Ni-M Hydride Electrode for Ni-MH Secondary Battery, J. Electrochem. Soc. 148 (2001) A1041–A1044.
[30] S. Han, M. Zhao, L. Wu, Y. Zheng, Effect of Additive Elements on Electrochemical Properties of $AB_2$-type Laves Phase Alloys, Chem. J. Chin. Univ. 24 (2003) 2256–2259.
[31] K. Petrov, A. Rostami, A. Visintin, S. Srinivasan, Optimization of Composition and Structure of Metal-Hydride Electrodes, J. Electrochem. Soc. 141 (1994) 1747–1750.
[32] H.M. Rietveld, A profile refinement method for nuclear and magnetic structures, J. Appl. Cryst. 2 (1969) 65–71.
[33] A.C. Larson, R.B. Von Dreele, General Structure Analysis System (GSAS), Los Alamos National Laboratory Report LAUR, 2000, pp. 86–748.
[34] B.H. Toby, J. Appl.Crystallogr. EXPGUI, a Graph. user interface GSAS 34 (2001) 210–213.
[35] K. Young, T. Ouchi, M.A. Fetcenko, Pressure–composition–temperature hysteresis in C14 Laves phase alloys: Part 1. Simple ternary alloys, J. Alloys Compd. 480 (2009) 428–433.
[36] K. Young, T. Ouchi, W. Mays, B. Reichman, M.A. Fetcenko, Pressure–composition–temperature hysteresis in C14 Laves phase alloys: Part 2. Applications in NiMH batteries, J. Alloys Compd. 480 (2009) 434–439.
[37] K. Young, T. Ouchi, M.A. Fetcenko, Pressure–composition–temperature hysteresis in C14 Laves phase alloys: Part 3. Empirical formula, J. Alloys Compd. 480 (2009) 440–448.
[38] W.K. Zhang, C.A. Ma, X.G. Yang, Y.Q. Lei, Q.D. Wang, G.L. Lu, Influences of annealing heat treatment on phase structure and electrochemical properties of $Zr(MnVNi)_2$ hydrogen storage alloys, J. Alloys Compd. 293–295 (1999) 691–697.
[39] Q.A. Zhang, Y.Q. Lei, X.G. Yang, K. Ren, Q.D. Wang, Annealing treatment of AB2-type hydrogen storage alloys: II. Electrochemical properties, J. Alloys Compd. 292 (1999) 241–246.
[40] F.C. Ruiz, E.B. Castro, S.G. Real, H.A. Peretti, A. Visintin, W.E. Triaca, Electrochemical characterization of $AB_2$ alloys used for negative electrodes in Ni/MH batteries, Int. J. Hydrogen Energy 33 (2008) 3576–3580.
[41] K. Young, T. Ouchi, B. Huang, B. Chao, M.A. Fetcenko, L.A. Bendersky, K. Wang, C. Chiu, The correlation of C14/C15 phase abundance and electrochemical properties in the $AB_2$ alloys, J. Alloys Compd. 506 (2010) 841–848.
[42] K. Young, J. Nei, B. Huang, M.A. Fetcenko, Studies of off-stoichiometric $AB_2$ metal hydride alloy: part 2. Hydrogen storage and electrochemical properties, Int. J. Hydrogen Energy 36 (2011) 11146–11154.
[43] J. Nei, K. Young, R. Regmi, G. Lawes, S.O. Salley, K.Y.S. Ng, Gaseous phase hydrogen storage and electrochemical properties of $Zr_8Ni_{21}$, $Zr_7Ni_{10}$, $Zr_9Ni_{11}$, and ZrNi metal hydride alloys, Int. J. Hydrogen Energy 37 (2012) 16042–16055.
[44] E.A. Ticianelli, S. Mukerjee, J. McBreen, G.D. Adzic, J.R. Johnson, J.J. Reilly, Reaction Kinetics, X-Ray Absorption, Spectroscopy Studies of Yttrium-Containing Metal Hydride Electrodes, J. Electrochem. Soc. 146 (1999) 3582–3590.
[45] A. Züttel, V. Güther, A. Otto, M. Bärtsch, R. Kötz, D. Chartouni, C.H. Nützenadel, L. Schlapbach, About the mechanism and the rate limiting step of the metalhydride electrode reaction, J. Alloys Compd. 293 (1999) 663–669.
[46] W. Zhang, M.P. Kumar, S. Srinivasan, H.J. Ploehn, Ac impedance studies on metal hydride electrodes, J. Electrochem. Soc. 142 (1995) 2935–2943.
[47] J. Chen, S.X. Dou, D.H. Bradhurst, H.K. Liu, Studies on the diffusion coefficient of hydrogen through metal hydride electrodes, Int. J. Hydrogen Energy 23 (1998) 177–182.
[48] J.E. Thomas, E.B. Castro, A. Visintin, Influence of the compaction pressure on the electrochemical impedance spectroscopy response of the $AB_5$-type electrodes, Int. J. Hydrogen Energy 35 (2010) 5981–5984.
[49] C. Wang, M. Marrero-Rivera, D.A. Serafini, J.H. Baricuatro, M.P. Soriaga, S. Srinivasan, The self-discharge mechanism of $AB_5$-type hydride electrodes in Ni/MH batteries, Int. J. Hydrogen Energy 31 (2006) 603–611.